Soft Matter

www.rsc.org/softmatter

Volume 8 | Number 33 | 7 September 2012 | Pages 8525–8796

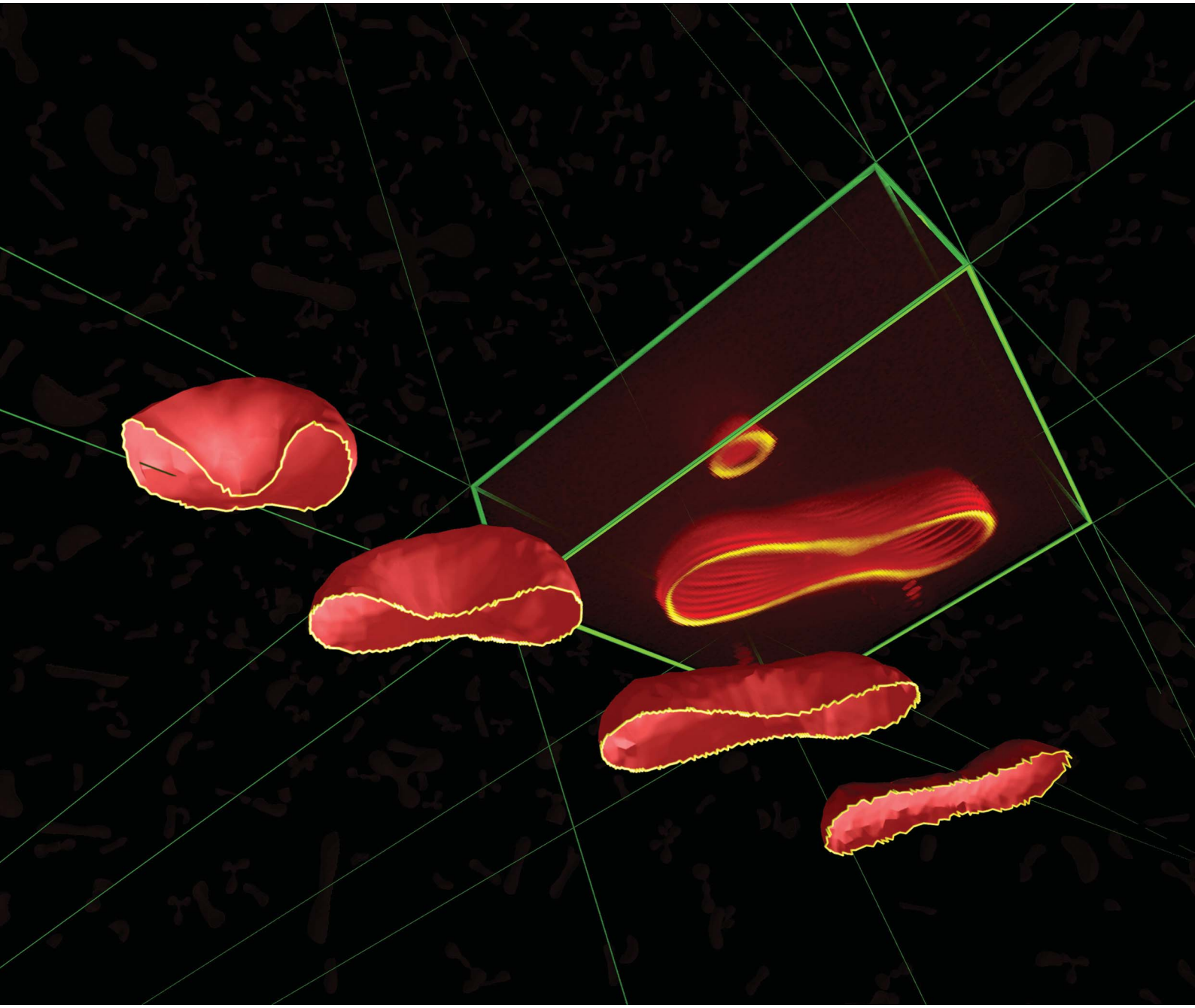

ISSN 1744-683X

RSC Publishing

PAPER

Primož Ziherl *et al.*

Three-dimensional analysis of lipid vesicle transformations

1744-683X(2012)8:33;1-8

Soft Matter

Dynamic Article Links

Cite this: *Soft Matter*, 2012, **8**, 8569

www.rsc.org/softmatter

PAPER

Published on 06 July 2012. Downloaded by Universitat Erlangen Nurnberg on 1/10/2020 8:46:35 AM.

Three-dimensional analysis of lipid vesicle transformations

Ai Sakashita,[a] Naohito Urakami,[b] Primož Ziherl*[cd] and Masayuki Imai[a]

Received 1st April 2012, Accepted 23rd May 2012
DOI: 10.1039/c2sm25759a

We use fast confocal laser microscopy to quantitatively study axisymmetric and nonaxisymmetric shapes of lipid vesicles undergoing spontaneous transformations. To characterize the observed three-dimensional shapes, we compute their respective reduced monolayer area difference and reduced volume. The transformations allow us to analyze a broad range of vesicle shapes including stomatocytes, elliptocytes, discocytes, cigars, necklaces, and many nonaxisymmetric shapes. The transformations are marked by a step-like time dependence of the reduced monolayer area difference, which is explained in terms of the area-difference-elasticity model. The simplest mechanism consistent with the observed shape transformations are small folded multilamellar patches on either monolayer. The experimental methodology validated by the reported results can be used to monitor and analyze more complex vesicle shapes and their evolution.

1. Introduction

Analysis and visualization of the shape of complex microscopic 3D biological objects is a difficult task. The standard 2D optical or electron microscopy provides an image of the cross-section of the object that may not capture many of its features. For example, the cross-sections of the Golgi apparatus seen in an electron microscope usually suggest that this organelle consists of a fairly ordered stack of pancake-like cisternae, but a reconstructed three-dimensional tomographic image reveals a much more sophisticated structure.[1] 3D imaging is indeed needed to fully comprehend the shape and the topology of many biological entities and for supra-micrometer objects such as whole cells, confocal microscopy has been the method of choice for many years.[2]

Taking a 3D image is merely the first step of an in-depth quantitative study. Image processing to extract the shape of the object is a considerable challenge best addressed with custom software tailored to the problem at hand. In this study, we developed and tested a new experimental methodology to analyze the shape of lipid vesicles as the simplest type of a biological compartment. Lipid vesicles were chosen as a suitable model system because they have been investigated quite thoroughly for over 30 years both experimentally[3–9] and theoretically.[10–13] Yet the spectrum of their shapes has not been completely explored, the most elusive ones being nonaxisymmetric shapes which occupy a large part of the phase diagram of more deflated vesicles.

The restricted quantitative insight into vesicle shapes is primarily due to the inherent limitations of 2D microscopy. Although indispensable in qualitative studies, 2D images can only be used to analyze axisymmetric vesicles provided that the representative cross-section lies in the focal plane (which can be achieved by relying on gravity[7]). By measuring the semiaxes of cross-section contour, one can determine the volume and the area of the spherical and ellipsoidal shapes[4] from which the reduced volume can be computed. In their landmark paper, Döbereiner and coworkers[7] used a series expansion to accurately describe the contours of axisymmetric vesicles that do not depart much from the sphere, and they related the coefficients of the expansion to both reduced volume v and reduced monolayer area difference Δa. This protocol works well for vesicles of large reduced volume where the expansion makes sense.[14] In the small-v regime, no systematic approach is known and one must resort to measuring the characteristic large features of vesicles such as arm number, length, and diameter in starfish,[6,15] height, diameter, and radius of invagination in stomatocytes, codocytes, and torocytes,[9] or semiaxes of ellipsoidal vesicles deformed by AC electric field.[16] Ratios of these lengths can then be used to compare experimental and theoretical shapes so as to estimate v and Δa of the former but the comparison is nontrivial because of thermal excitations.[17,18]

Confocal microscopy does not suffer from some of the issues affecting the functionality of 2D microscopy of vesicles and it produces 3D images of appropriate spatial resolution, which makes it suitable for a detailed quantification of the shape of vesicles. The purpose of this work is threefold. Our central goal was to develop a methodology for processing and analysis of

[a]*Department of Physics, Ochanomizu University, 2-1-1 Otsuka, Bunkyo, Tokyo, 112-8610, Japan*
[b]*Department of Physics and Information Sciences, Yamaguchi University, 1677-1 Yoshida, Yamaguchi, 753-8512, Japan*
[c]*Faculty of Mathematics and Physics, University of Ljubljana, Jadranska 19, SI-1000 Ljubljana, Slovenia*
[d]*Jožef Stefan Institute, Jamova 39, SI-1000 Ljubljana, Slovenia. E-mail: primoz.ziherl@ijs.si; Fax: +386 1 4773 724; Tel: +386 1 4773 613*

Published on 06 July 2012. Downloaded by Universitat Erlangen Nurnberg on 1/10/2020 8:46:35 AM.

vesicle images from a fast confocal microscope. Secondly, the methodology was put to test by extracting the morphometric parameters of many isolated lipid vesicles and arranging them in the phase diagram. In addition, we studied spontaneous shape deformations of the vesicles, thereby recreating the transformation pathways reported in ref. 9 and those induced by changing the temperature.[4,19] We observed several types of trajectories transforming, *e.g.*, prolate vesicles to invaginated shapes or *vice versa*. Also seen were bidirectional transformations where, *e.g.*, a necklace-like budded shape is spontaneously deformed into a cigar and then into a discocyte to finally evolve to a budded starfish-like structure. The new experimental methodology was instrumental for the detailed quantification of these transformations because it provided a means to examine the many nonaxisymmetric shapes involved.

Finally we compared the experimental shapes with those predicted by the bilayer-couple (BC) model[11] to find that they agree very well, which means that the spontaneous shape deformations are quasi-static. Thus we can use them to scan the phase diagram of vesicles, which is consistent with the area-difference-elasticity (ADE) theory.[14,20] In this respect, our study is related to ref. 7 except that our methodology is not restricted to axisymmetric shapes and large reduced volumes. Moreover, we find that the transformation pathways consist of a sequence of BC shapes connecting two adjacent stable shapes.

The disposition of the paper is as follows. In Section 2 we describe the experimental protocols used including vesicle preparation, image processing and analysis, and in Section 3 we report our experimental observations of vesicle shapes and their transformations. Section 4 discusses the results from the theoretical perspective in terms of the ADE model. We conclude the paper by summarizing the findings and by outlining their relevance for further studies.

2. Experimental

2.1. Samples

DOPC (1,2-dioleoyl-*sn-glycero*-3-phosphocholine) was obtained as a powder from Avanti Polar Lipids. The purity of the lipid indicated by the manufacturer was 99%, and the transition temperature is −20 °C. The lipid was dissolved in chloroform (at a concentration of 2 mmol l^{-1}) and stored at −18 °C. TR–DHPE (Texas Red, 1,2-dihexadecanoyl-*sn-glycero*-3-phosphoethanolamine) was obtained as a powder from Molecular Probes. It was dissolved in chloroform at 0.72 mmol l^{-1} and we used as the fluorescent dye.

2.2. Preparation of vesicles

To prepare giant vesicles, we used the gentle hydration method with pure water.[21,22] First we mixed 50 μl of the solution, 1.5 μl of TR–DHPE and 750 μl of chloroform in a bottle. The bottle was cleaned by a mixture of chloroform and methanol (volume ratio of 2 : 1). Then we dried this solution using gaseous nitrogen to make the lipid film and incubated it in vacuum for 1 day. We wrapped the bottle in aluminum foil to protect it from ambient light. Then we hydrated the sample with 2 ml of pure water at room temperature (24–25 °C) for 1 h to produce vesicles. Most vesicles had either a spherical or a tubular shape, which was subsequently controlled by applying osmotic pressure. We put 90 μl of the vesicle solution on a glass slide and added 10 μl of sorbitol (Sigma Aldrich, 20 mmol l^{-1}) to apply a concentration difference of 2 mmol l^{-1}. Within 1 min, this small osmotic pressure difference led to a decrease of vesicle volume and an ensuing deformation from a sphere to an oblate or a prolate shape. After that, the volume of these shapes no longer changed. We waited for another 5 min until the solution was abundant with many different vesicles, and then we started to observe their spontaneous shape deformations.

2.3. Observation

As the vesicles were dispersed in water, their position and orientation fluctuated constantly. In addition, the motion of vesicles was affected by continuous evaporation of solvent, the magnitude of fluctuations was smallest in the center of the cover glass. In order to record the shape as accurately as possible, we studied large vesicles that were over 20 μm whose typical speed in the xy plane did not exceed 2 μm s^{-1}. Fast imaging was done using a high-speed confocal laser scanning microscope (Carl Zeiss, LSM 5Live) with water immersion objective (C-Apochromat 63×/1.20 W Korr UV-VIS-IR). We used a He–Ne laser with a wavelength of 532 nm. With our setup, a vesicle can be scanned within a period of 1 or 2 s, the duration depending on the size of the images and resolution in the z direction. We set the slit width to the minimal value of 16.6 μm so that the resolution in the z direction was finest. In this case, our three-dimensional vesicle images consisted of about 100 two-dimensional xy slices of frame size 100 μm × 50 μm separated by 0.55 μm (Fig. 1a).

The temporal resolution of the experiment was determined by several factors. The main criterion was the rate of the shape transformation of the vesicles, which typically took from 10 to 20 s to complete. In order to record it accurately, the delay between successive images should not be too long. In our experiment, the delay was set to 2.5 s—short enough so that the vesicles did not move too much during this interval which facilitated tracking. The main technical issue related to the temporal resolution was the deterioration of dye caused by the laser light. To minimize this effect, we used as low a power as possible, which in turn meant a relatively long irradiation time of 2 s. This was consistent with the desired longest delay mentioned above. The typical total observation times were between 100 and 200 s.

After taking an image, we processed it using the microscope software LSM Image Browser (Carl Zeiss). This software has several built-in functions, which were used to measure the size of the vesicle and to construct its three-dimensional shape (Fig. 1a).

2.4. Image processing

The distribution of fluorescence intensity in a typical vesicle image is fairly nonuniform. Since the vesicles are illuminated by laser light from below, the bottom part of the vesicle is brightest. In addition, when the laser shines on a part of the vesicle, the dye fluoresces brightly. In turn, this light is reflected from surroundings so that the exact location of the illuminated part of membrane is obscured. If the brightness of the image were uniform, we could determine the vesicle shape easily but in most vesicles this is not the case.

 This journal is © The Royal Society of Chemistry 2012

Published on 06 July 2012. Downloaded by Universitat Erlangen Nurnberg on 1/10/2020 8:46:35 AM.

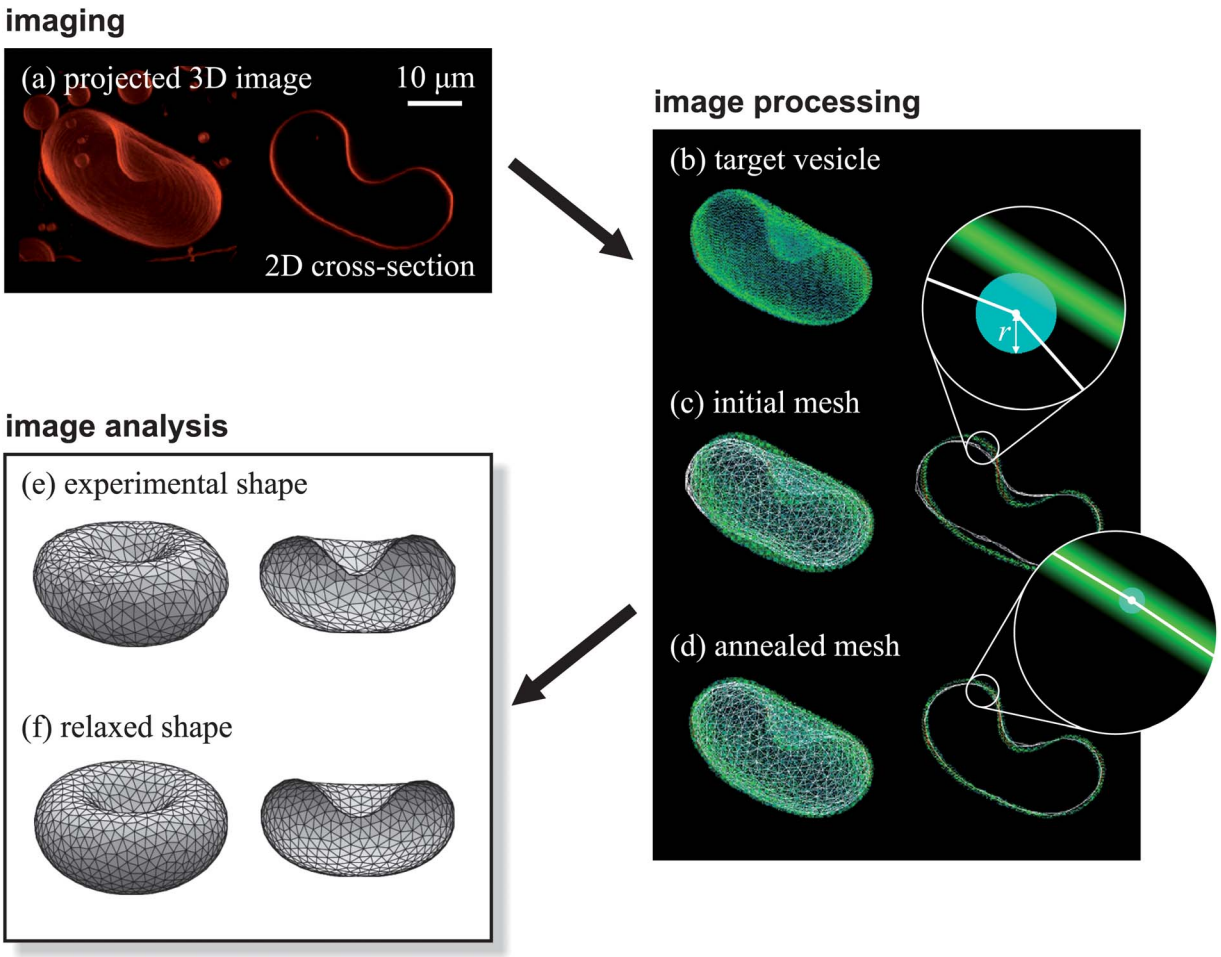

Fig. 1 Imaging, image processing, and image analysis. The three-dimensional confocal microscope image (panel a) consists of a sequence of two-dimensional *xy* cross-sections of vesicles. The first stage of processing is isolation of the target vesicle by removal of all other vesicles and its conversion of the image into a binary format (b). The shape of the target vesicle is extracted by superposing the initial mesh (c; white) onto the binary image. Ideally, the initial mesh is not very different from the shape studied, which is best seen in cross-section. During annealing, the mesh nodes (white dot in the two schematics) approach the brightest part of the membrane. In each step, the brightest voxel close to a node is searched for within the sphere of radius *r* (cyan circle). The final mesh agrees well with the experimental image: Panel (d) shows the whole vesicle with the mesh and their cross-sections. Note that *r* is decreased in the final stages of annealing. In the image analysis, the final mesh is converted into the Surface Evolver format (e; shown here are the three-dimensional projection and the cutaway view). The raw shape is then relaxed at fixed vesicle area, volume, and integral mean curvature to minimize the Helfrich local bending energy, which removes artifacts of image processing and produces a faithful representation of the original image (f).

In order to obtain the surface of the target vesicle, we developed a computer program for image analysis. First we converted the images of the *xy* sections to fluorescence intensity data and merged all of them into a 3D image. This format is suitable for further numerical analysis, and it includes the coordinates (x, y, z) and the fluorescence intensity I $(0 \leq I \leq 255)$. At this stage, the field-of-view around the target vesicle typically contains many other vesicles. To isolate the target, we removed the nearby vesicles based on the connectedness of the data. The fluorescence intensity image of the target vesicle from Fig. 1a is shown in Fig. 1b.

Then we extracted the vesicle surface. In this step, we had to deal with the uneven brightness of the surface described above. To obtain a continuous vesicle surface without any gaps or holes, we chose a low value of the intensity threshold that signals the presence of the membrane. Depending on the vesicle, the threshold was set at a value between three and five times the average intensity across all of the volume containing the vesicle, and it typically ranged from 15 to 30 on a 0 to 255 intensity scale. But this procedure raised other issues. A patch of the vesicle surface is reflected from the neighboring parts of the membrane or from a nearby vesicle and we cannot distinguish between the actual patch and its mirror images produced by reflections. This problem is most severe in stomatocytes of small reduced volumes where the invaginated part of the membrane closely approaches the opposite side of the vesicle. We minimized the impact of this effect by selecting target vesicles that were far from others and whose orientation relative to laser beam was favorable.

The vesicle shape was extracted by superposing a triangular mesh onto experimental fluorescence data. The mesh consisted of a set of nodes, each of them characterized by an identification number, spatial coordinates, number of neighbors, and their identification numbers. These data define the connectivity of the mesh. In our experience, about 600 nodes were sufficient to

Published on 06 July 2012. Downloaded by Universitat Erlangen Nurnberg on 1/10/2020 8:46:35 AM.

accurately describe the large, average features of vesicles; a coarser mesh would not capture the vesicle shape well enough, whereas a finer resolution is too sensitive to shape fluctuations.

First we created a mesh whose shape was close enough to that of the target vesicle (Fig. 1c) and we superimposed it over the vesicle surface. The initial mesh was generated using the Surface Evolver package[23] (hereinafter called SE), a freely available software for numerical studies of various mechanical systems of reduced dimensionality, *e.g.*, soap films. Within SE, the parameters of the initial mesh such as enclosed volume, area, shape, and orientation can be varied easily. Shapes similar to the observed vesicles were created routinely and then converted into the format used by our custom image-processing program.

Next we let the mesh snap to the vesicle surface distinguished by a higher local intensity than the adjacent parts of image. This was done by introducing an auxiliary potential U_i which drove the mesh towards the vesicle surface; two additional auxiliary elastic energies described below were employed to ensure that the mesh is reasonably smooth and equally spaced.

We fitted the mesh to the fluorescence distribution as closely as possible using Monte Carlo stimulated annealing (Fig. 1d). In order to locate the surface, we picked the brightest part in a small spherical volume centered around node i (Fig. 1c and d). The auxiliary potential energy of the node i is given by the sum of the intensity of all voxels whose distance to node i is less than r:

$$U_i = -\sum_{j=1}^{M} I_j. \tag{1}$$

Here j is the index of image voxels and M is number of voxels within the sphere of radius r centered at node i. Radius r is determined by the thickness of the membrane h (from 5 to 15 voxel edge lengths). In the initial stage of relaxation, we used a large r (between 3 and 7 voxel edge lengths) to let the mesh approach the fluorescence image, and then we gradually decreased it for a closer fit such that finally $r \approx h/2$ (*i.e.*, between 2 and 5 voxel edge lengths; Fig. 1c and d). The total potential energy of the mesh is $U_0 = \sum_{i=1}^{N} U_i$, where N is the number of nodes (typically about 600).

To obtain a smooth representation of the vesicle, we resorted to an auxiliary elastic energy of the mesh represented by a system of harmonic springs

$$U_s = \frac{1}{2} k_1 \sum_{i=1}^{N} \sum_{j=1}^{n} (d_{ij} - d_0)^2, \tag{2}$$

where k_1 is the spring constant, j is the index of a neighbor of node i, d_{ij} is the distance between nodes i and j, n is the number of neighbors of node i, and d_0 is the average length of bonds measured in units of voxel edge length. Typical values of d_{ij} and d_0 ranged from 3 to 15 voxel edge lengths depending on vesicle size. Equidistant spacing of nodes was promoted by including a term that penalizes a deviation of the position of i^{th} node $\mathbf{R}_i$ (measured relative to the origin at the center of vesicle mass) from the center of mass of its neighbors $\overline{\mathbf{R}}_i = (1/n)\sum_{j=1}^{n} \mathbf{R}_j$, where j runs over all neighbors. This term reads

$$U_e = \frac{1}{2} k_2 \sum_{i=1}^{N} (\mathbf{R}_i - \overline{\mathbf{R}}_i)^2, \tag{3}$$

where k_2 is the elastic constant.

To fit the mesh to the intensity data, the potential and the elastic energy were minimized using two types of Monte Carlo moves. The first one is translation: here we let each node move a little in a random manner such that $\mathbf{R}_i^{\text{new}} = \mathbf{R}_i^{\text{old}} + \Delta\mathbf{R}_i$, where $\Delta\mathbf{R}_i$ is a random displacement of magnitude no larger than $0.1d_0$. The second type of move is scaling where the whole mesh is isotropically deflated or inflated: $\mathbf{R}_i^{\text{new}} = s\mathbf{R}_i^{\text{old}}$. Here s is the scaling parameter which should not depart too much from 1. We chose it randomly in the range $0.9 \leq s \leq 1.1$. This transformation was applied to all nodes simultaneously so that all bond lengths were scaled too. By affecting globally the whole mesh in a single step, it facilitated a faster relaxation of the mesh.

The random trial moves were accepted based on the Metropolis algorithm where the acceptance probability is given by $w = \min(\exp(-\beta\Delta U, 1))$. Here $\Delta U = \Delta(U_0 + U_s + U_e)$ is the energy difference of the final and the initial state and β is the inverse annealing temperature. Depending on the shape in question, we used various annealing cycles. All of them relied primarily on translation of individual nodes as the basic move, whereas inflation/deflation was applied only occasionally.

The typical cycle consisted of 250 moves per node and we repeated it about 5 times while β was increased in a stepwise fashion from 0.1 to 0.3. The spring constant k_1 was increased simultaneously from 20 to 40 and k_2 was also increased from 40 to 80, which increased the relative weight of the elastic terms compared to the potential energy. This protocol produced a two-stage annealing process. The first, small-β stage is characterized by large displacements where the mesh approached the brightest parts of the image, whereas in the second, large-β stage the mesh effectively became more smooth. The absolute values of the potential energy, elastic constants and the annealing temperature are, of course, irrelevant. Their values were chosen such that towards the end of annealing, the acceptance rate for the moves with $\Delta U > 0$ was negligible. In our experience, the thus generated meshes captured the actual shapes of vesicles well.

2.5. Image analysis

After extracting the vesicle shapes from the confocal micrographs using our image-processing program, we converted them into SE format for quantitative analysis. The main advantage of using SE are the many functions and procedures for the manipulation of surfaces and their evolution due to action of various types of forces which include bending stresses. Within the SE package, we can readily evaluate vesicle volume V and area A as well as the difference of areas of the two monolayers which is proportional to integrated mean curvature

$$\Delta A = h \oint (C_1 + C_2) \mathrm{d}A. \tag{4}$$

Here h is the distance between monolayers' neutral planes, C_1 and C_2 are the two curvatures, and the integral goes over the vesicle surface. These three extensive quantities are then combined into two parameters that parametrize the vesicle shape: the reduced volume v

$$v = \frac{V}{4\pi R_s^3/3}. \tag{5}$$

 This journal is © The Royal Society of Chemistry 2012

Published on 06 July 2012. Downloaded by Universitat Erlangen Nurnberg on 1/10/2020 8:46:35 AM.

(where $R_s = \sqrt{A/4\pi}$) and the reduced monolayer area difference

$$\Delta a = \frac{\Delta A}{8\pi h R_s}. \quad (6)$$

For example, in the shape shown in Fig. 1b $v = 0.79$ and $\Delta a = 0.98$; its SE 3D projection and cutaway view are shown in Fig. 1e. We estimated the experimental error of the two shape parameters by repeated processing of the same image with somewhat different parameters of our image analysis program. By comparing the results, we concluded that the typical absolute measurement errors of both quantities were about 0.01 except in some shapes at small reduced volumes ≈ 0.5 where it reached 0.02.

After computing the vesicle reduced volume and reduced monolayer area difference, we used SE to relax the shape to minimize the Helfrich bending energy[10] at fixed nominal v and Δa

$$W_b = \frac{k_c}{2}\oint (C_1 + C_2)^2 \mathrm{d}A, \quad (7)$$

where k_c is the local bending constant; this bending energy and the two constraints constitute the BC model.[11] The relaxation did not alter the large features of the shapes but it removed most of the surface corrugation introduced by image processing and produced faithful representations of confocal micrographs (Fig. 1f), the few remaining discrepancies being restricted to small-scale details.

3. Results

After the lipid films were rehydrated, many vesicles formed spontaneously. In the 100 μm × 100 μm field-of-view, there were typically more than 10 vesicles of various shapes, sizes, and topologies. We chose to examine the most interesting vesicles without any holes or handles. Given the spatial resolution of the microscope, we studied vesicles bigger than 15 μm whose shape can be captured accurately enough by our microscope.

The vesicles typically drifted slowly across the field of view and their orientation in space was unsteady too. But the 3D scanning capability of the microscope rendered these motions unimportant so that we could concentrate on vesicle shape. In our experiment, many axisymmetric (cigars, pearl necklaces, discocytes, stomatocytes, pears, …) and nonaxisymmetric (rackets, starfish, elliptocytes, …) shapes of various reduced volumes were observed and monitored. Most vesicles studied had a reduced volume between 0.5 and 0.7. In this regime the spectrum of shapes is diverse enough but the shapes themselves are not too elaborate and difficult to analyze.

The first observation is that the vesicle shape changed spontaneously with time. The rate and the sense of transformation was not the same in all vesicles and it did not seem to depend on their size. In all shape transformations the reduced volume of the vesicles stayed virtually constant on the timescale of shape transformations which usually took about 200 s. Thus the reduced monolayer area difference Δa remained the main time-dependent shape parameter.

Shape transformations that we observed can be divided into three classes according to the way Δa changed with time. In the first class of transformations Δa decreased with time. Some of these transformations included an elaborate shape sequence (*e.g.*, the cigar → racket → discocyte → stomatocyte transformation shown in Fig. 2a) and in some only two shapes were involved (*e.g.*, necklace → cigar transformation). The sequence of shapes involved depended on the reduced volume as expected based on theoretical predictions.[24] Also important was the initial shape. Starfishes readily transformed into discocytes and then into stomatocytes but in the cigar–stomatocyte transformation which was mediated by rackets and discocytes, starfishes were bypassed.

The second class of transformations were those where Δa increased with time. Many times we observed the cigar–necklace transition (such as that seen in Fig. 2a). A more elaborate transformation of this type is the stomatocyte → discocyte → triangular oblate shape → cigar sequence (Fig. 2b).

Sometimes both classes of transitions were combined in a single sequence. For example, a necklace–stomatocyte transformation *via* cigars, rackets, and discocytes was followed by a stomatocyte–necklace transformation involving discocytes, triangular oblate shape, and three-arm starfish. These

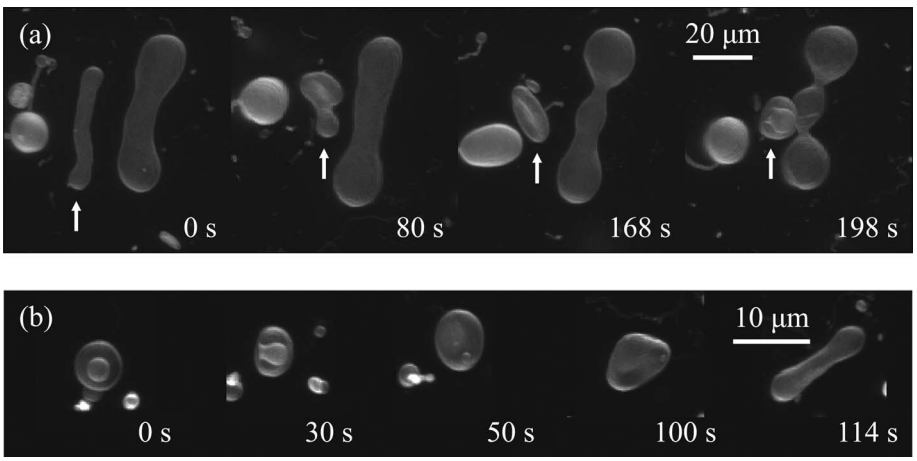

Fig. 2 Shape deformation of two nearby cigar vesicles. The smaller cigar in panel (a) marked by the arrow transformed into a stomatocyte *via* a racket shape and a discocyte, whereas the larger cigar evolved into a three-pearl necklace. Panel (b) shows snapshots of a stomatocyte–cigar transformation proceeding in the opposite direction as the transformation of the smaller vesicle in panel (a). In this case, the intermediate shape between the discocyte and the cigar is a triangular oblate shape rather than the racket shape seen in panel (a), which suggests that this transition is discontinuous.[24] The timescales of both transformations are very similar. These sequences demonstrate that either direction of shape deformations is possible.

Published on 06 July 2012. Downloaded by Universitat Erlangen Nurnberg on 1/10/2020 8:46:35 AM.

bidirectional trajectories constitute the third class of shape transformations and they were marked by a shape hysteresis. Many ended at a Δa that was very close to that of the starting shape but the final shape was different from the initial one. For example, an initially cigar-shaped vesicle transformed *via* racket-like shapes directly into a discocyte, which subsequently evolved into a starfish rather than back to the cigar. It seems that the final part of each leg of the cycle included metastable rather than stable shapes. The bidirectional transformations were only observed at v smaller than about 0.6.

In our experience, there is no obvious cause deciding the direction of the shape transformation of a certain vesicle. In some cases, two nearby vesicles of similar size which clearly resided in the same local environment evolved in the opposite directions. The two cigar-shaped vesicles shown in Fig. 2a were initially rather similar in shape. After a while, the smaller cigar started transforming such that Δa was decreased. It first evolved into a racket, then to a discocyte and finally to a stomatocyte. On the other hand, the larger vesicle was simultaneously transformed from a cigar to three-pearl necklace consistent with an increase of the reduced monolayer area difference.

The arbitrariness of the direction of the shape transformation is further illustrated by Fig. 2b which shows a sequence of snapshots illustrating the stomatocyte–cigar transformation. Although seen less often than the cigar–stomatocyte transformations discussed in detail below, such events prove that the shape transformations can proceed in either direction.

In the following, we describe the shapes and the shape transformations quantitatively. As mentioned in Section 2.5, the last step of our image analysis was shape relaxation to minimize the Helfrich bending energy [eqn (7)], which was done within SE at a fixed nominal reduced volume and reduced monolayer area difference. In almost all cases, the relaxation rendered the shapes more smooth without affecting their salient features, which is illustrated by a selection of representative observed vesicles along with the corresponding theoretical shapes computed within the BC theory (Fig. 3). The axisymmetric shapes shown in Fig. 3 have been quantified long ago but the many nonaxisymmetric vesicles such as the triangular shape (Fig. 3b) were not. All shapes fluctuated due to thermal excitation, and some were characterized by slow modes. The most typical mode of the starfish vesicles with long protruding arms was the extension of one arm at the expense of another. This has been reported earlier, the reason being the degeneracy of energies of starfishes whose sum of arm lengths is constant.[15] The other prominent low-energy fluctuation mode is the bend mode of the elongated shapes seen in the cigar (Fig. 3c) and the elliptocyte (Fig. 3e).

As shown below, shape transformations observed here include shapes that persist for several tens of seconds or longer (Fig. 3a, c, d, and f) and transient shapes which evolve at a much shorter timescale, typically of the order of 1 s (Fig. 3b and e). We stress that both the persistent and the transient shapes are consistent with the BC model. This is a very important conclusion because it suggests that the spontaneous shape deformations were slow enough for the vesicles to reach mechanical equilibrium. The shape deformation process is thus quasistatic.

To comprehensively demonstrate the agreement of the observed vesicles with the BC model, we arranged a total of 197 analyzed shapes of reduced volume between 0.5 and 1 in the

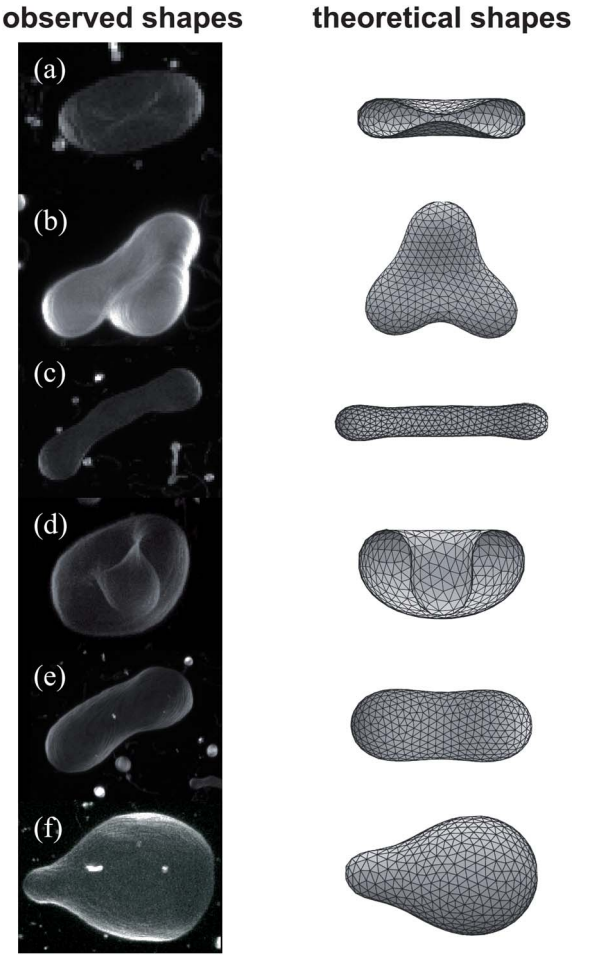

Fig. 3 Selected vesicles compared to stationary shapes computed within the BC model: Discocyte (a; $v = 0.51$, $\Delta a = 1.05$), triangular oblate shape (b; $v = 0.53$, $\Delta a = 1.24$), cigar (c; $v = 0.54$, $\Delta a = 1.52$), stomatocyte (d; $v = 0.58$, $\Delta a = 0.77$), elliptocyte (e; $v = 0.68$, $\Delta a = 1.22$), and pear (f; $v = 0.91$, $\Delta a = 1.07$). The theoretical shapes are rotated so as to expose their representative cross-sections; the discocyte and the stomatocyte are shown in cutaway view. The agreement of the theoretical and the experimental shapes is remarkably good, both in the persistent shapes which remain stable for several tens of seconds (a, c, d, and f) and in the transient shapes which deform at the timescale of seconds (b and e). The elliptocyte (c) and the cigar (e) depart somewhat from the energy-minimizing axisymmetric shape due to long-wavelength thermal bend modes.

phase diagram (Fig. 4; some of the datapoints coincide). We focus on the central part of the diagram which is dominated by the nonaxisymmetric shapes involved in the transition between the discocytic and the axisymmetric prolate vesicles. Each point represents a shape characterized by the measured v and Δa. Also included are the theoretical BC model boundaries: line S represents the continuous stomatocyte–discocyte transition, whereas line C indicates the location of the cigar shapes.[14,24] Non-axisymmetric shapes are stable within the wedge-like region between lines S and C.

The experimental datapoints nicely coincide with theory. In case of stomatocytes and discocytes, the agreement is very good and the hierarchy of nonaxisymmetric shapes—elliptocytes at v larger than about 0.6, and triangular oblate shapes, three-arm

 This journal is © The Royal Society of Chemistry 2012

Published on 06 July 2012. Downloaded by Universitat Erlangen Nurnberg on 1/10/2020 8:46:35 AM.

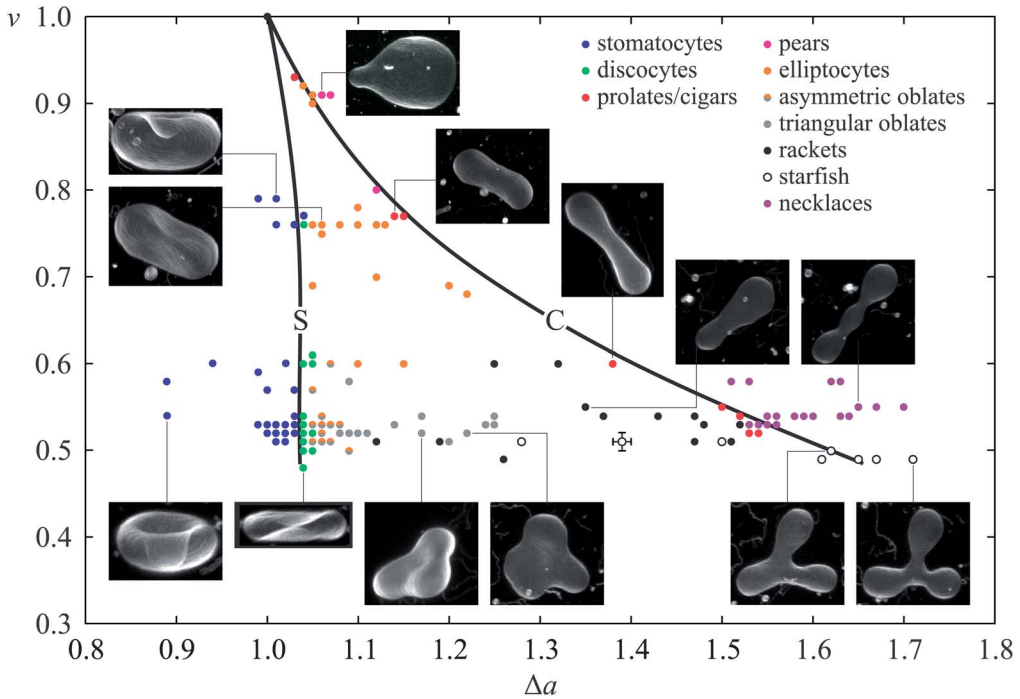

Fig. 4 Vesicle phase diagram in the (v, Δa) plane. The different classes of shapes are color-coded and the main features of the experimental diagram agree well with the theoretically predicted boundaries represented by the two solid lines which indicate the stomatocyte–discocyte transition (S) and the location of the cigar shapes (C; adapted from ref. 14 and 24). The most systematic departure of the experimental shapes from the theory is at v between 0.5 and 0.6 and Δa between 1.04 and 1.1 where the observed shapes are oblate and asymmetric but lack the predicted triangular contour. Also included are snapshots of some representative shapes. Error bars corresponding to an absolute uncertainty of ± 0.01 are indicated at one of the datapoints at the bottom of the diagram.

starfish, and rackets at v smaller than 0.6—is also consistent with the predictions.[24] In a small region of the phase diagram at v between 0.5 and 0.6 and Δa between 1.04 and 1.1, the observed vesicles agree with the theoretical shapes in that they are oblate and nonaxisymmetric but they lack the triangular appearance of the theoretical shapes. We refer to these shapes as asymmetric oblates. Also included in the phase diagram are the spherical shape at $v = 1$, $\Delta a = 1$, a few pear shapes found at large v, and several three-pearl necklaces at $v \approx 0.55$ and $\Delta a > 1.5$ in the rightmost part of the diagram. Not all of the necklace shapes are as articulated as the one shown in the snapshot in Fig. 4; in those lying close to line C the necks are less well-developed.

The data at reduced volume of around $v = 0.53$ suggest that the discocyte–cigar transition is indeed discontinuous as predicted theoretically.[24] The triangular oblate shapes at Δa between 1.1 and 1.3 and the rackets at Δa between 1.35 and 1.55 belong to different symmetry classes. Some of these shapes must be metastable rather than stable, which is further supported by the two groups of outliers at $v \approx 0.5$ at the bottom. Both the rackets at Δa between 1.1 and 1.3 and the starfish at Δa between 1.6 and 1.7 were obtained by driving the two stable branches beyond the starfish–racket transition at $\Delta a \approx 1.52$.[24] This argument may also explain the existence of the reported $v = 0.5$ and $v = 0.51$ asymmetric oblate shapes which evolved from rackets during the cigar–discocyte transition.

Next we turn to the shape deformation process itself. Three representative examples of the cigar-to-stomatocyte transformation encoded by the time dependence of v and Δa are shown in Fig. 5. The initial shape of these vesicles of reduced volumes of $v = 0.76$, 0.60 and 0.51 was a cigar; the cigar stages correspond to the plateaux at $\Delta a \approx 1.15$, 1.38 and 1.53, respectively, and the starting time $t = 0$ of the observation is arbitrary. After a period of the order of 1 min, the three cigars started to gradually transform into discocyte shapes marked by $\Delta a \approx 1.04$. In all three cases, the cigar–discocyte transformation took about 10 s to complete and occurred *via* a continuous sequence of nonaxisymmetric shapes including elliptocytes (numerically computed nominal $v = 0.76$) and rackets ($v = 0.60$ and $v = 0.51$). The vesicles retained a

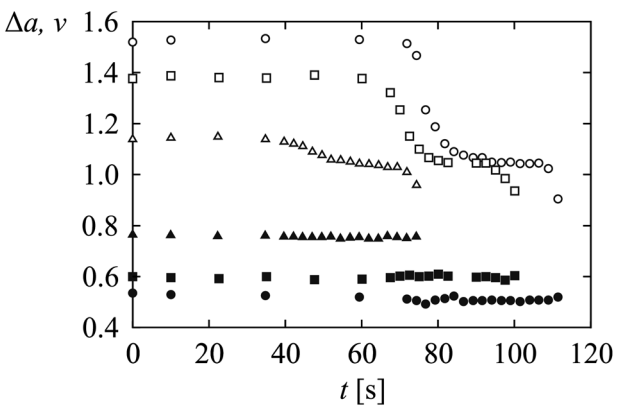

Fig. 5 Three cigar–stomatocyte transformations represented by vesicle reduced volume v (filled symbols) and reduced monolayer area difference Δa (open symbols) *vs.* time. Shown here are the shape sequences for vesicles of nominal $v = 0.76$, 0.60 and 0.51 (triangles, squares, and circles, respectively). These shape transformations took place at a virtually constant reduced volume.

Published on 06 July 2012. Downloaded by Universitat Erlangen Nurnberg on 1/10/2020 8:46:35 AM.

discocytic shape for around 20 s and after that their shape changed again, this time to a stomatocyte. During the shape transitions, v stayed almost constant.

The shape transformations shown in Fig. 5 are the simplest types of spontaneous vesicle evolution that we observed. Before discussing the more complicated examples, it is instructive to outline how they can be interpreted in terms of the ADE theory.

4. Discussion

The most prominent feature of the observed shape transformations is their step-like progression. This could result from a staggered time variation of the parameter that controls the vesicle shapes or from a discontinuous dependence of the vesicle shape on this parameter, which could then change more gradually with time. In view of the ADE theory of vesicle shapes where the transitions between stable shapes are generally discontinuous, the latter possibility seems more likely. As this scenario has been proposed earlier,[9] we will merely sketch its main elements.

In the ADE theory, the local bending energy W_b is complemented by the so-called non-local bending energy associated with the relative stretching of the monolayers in the membrane.[20] If the monolayer area difference ΔA [eqn (4)] departs from some preferred value ΔA_0, which is determined by the number of lipid molecules in the two monolayers, the monolayers are stretched relative to one another and the energy is increased by

$$W_r = \frac{k_r}{2Ah^2}(\Delta A - \Delta A_0)^2. \quad (8)$$

Here k_r is the non-local bending modulus†. The stable shapes minimizing $W_b + W_r$ depend on the ratio of the bending moduli

$$q = \frac{k_r}{k_c}, \quad (9)$$

which is typically around 3.[9,25] The reduced local and non-local bending energies are conventionally measured relative to the bending energy of a sphere: $w_b = W_b/8\pi k_c$ and $w_r = W_r/8\pi k_c$, respectively. The reduced preferred monolayer area difference is defined by $\Delta a_0 = \Delta A_0/8\pi h R_s$.

The ADE model establishes the relative stretching of monolayers as an independent mode that competes with the global shape determined by the local bending energy alone. This competition is possible because w_b is a fairly complicated function of the reduced monolayer area difference Δa, characterized by several pronounced local minima.[11,14,24] If q is not too big, a shape with a given $\Delta a'$ is energetically favorable compared to a shape with some other Δa provided that $w_b(\Delta a) - w_b(\Delta a') > q(\Delta a - \Delta a')$.[2]

Within the ADE model, Δa_0 can be considered as a generalized external force that controls the shape encoded by Δa, and Δa plays the role of a generalized coordinate.[20] The shape sequence minimizing the ADE energy

$$w_{ADE}(\Delta a_0) = \min_{\Delta a}\left(w_b(\Delta a) + w_r(q; \Delta a_0, \Delta a)\right) \quad (10)$$

consists of a subset of BC shapes; those left out are typically outweighed by one of the shapes corresponding to a local minimum of w_b. If q is small, the shape sequence is dominated by the stomatocyte, the discocyte, and the cigar.[13]

The main qualitative feature of the ADE phase diagram in the $(v, \Delta a_0)$ plane is that the transitions between the different shapes are generally discontinuous.[11,13] This is illustrated in Fig. 6a where the $v = 0.53$ BC bending energy $w_b(\Delta a)$ is used to construct the corresponding ADE shape sequences for $q = 2$ and $q = 3$. The importance of the non-local bending energy w_r is most apparent at Δa_0 around 1.04 representing the discocyte where the combined local and non-local bending energy of the discocyte is considerably smaller than the local bending energy of shapes of Δa close to, but different from 1.04. The other outstanding shape is the cigar at $\Delta a = 1.53$.

In case $q = 3$, the energy-minimizing shape sequence consists of a limiting stomatocyte shape‡ consisting of two spheres stable at Δa_0 smaller than approximately 0.55 followed by a continuous sequence of stomatocyte shapes which undergo a continuous transition to the discocyte at $\Delta a_0 \approx 1.01$. The discocyte is stable in a broad range of Δa_0 but at $\Delta a_0 \approx 1.26$ it is replaced by the triangular oblate shapes. At $\Delta a_0 \approx 1.46$ these shapes experience a discontinuous transition to the cigar shape. These transitions are easily discernible in Fig. 6b where Δa is plotted as a function of Δa_0. By comparing $\Delta a(\Delta a_0)$ for $q = 3$ and $q = 2$ we see that as the ratio of non-local and local bending constants is increased, the discontinuous transitions between the different shapes become less prominent. In the limit of $q \to \infty$, they vanish altogether and Δa is equal to Δa_0.

The step-like profiles of $\Delta a(\Delta a_0)$ shown in Fig. 6b are qualitatively reminiscent of the observed trajectories of shape deformations (Fig. 5) if one assumes that Δa_0 decreases with time. In particular, the cigar and the discocyte plateaux of the theoretical $v = 0.53$ trajectory at $\Delta a \approx 1.53$ and 1.04, respectively, agree with Fig. 6b which shows $\Delta a(t)$ of the vesicle with nominal 0.51; the discrepancy between the adjusted $v_{ad} = 0.53$ and the nominal $v = 0.51$ is a little bigger than the estimated average experimental error mentioned in Section 2.5. The experimentally observed cigar–discocyte transition is continuous rather than discontinuous, as predicted by the ADE theory but this is to be expected because it has to be physically accomplished by a certain transformation pathway which involves material motion associated with viscous damping. We conclude that the evolution of vesicles shown in Fig. 5 is consistent with the ADE theory.

4.1. Time dependence of Δa_0

Extracting the time dependence of the preferred monolayer area difference Δa_0 from the observations is difficult. In the three sequences shown in Fig. 5 it obviously decreases with time, but it is far less clear whether this takes place at a steady rate or not—and if not, what exactly is $\Delta a_0(t)$. The main features that we should try to reproduce are the durations of the cigar and the discocyte phases. The cigar phases present a difficulty because we do not know when did they begin; we only know that they lasted for more than about 35 s ($v = 0.76$), 60 s ($v = 0.60$), and 70 s ($v = 0.51$). The end of the cigar phases can be associated with the beginning of the decrease of Δa. Although Fig. 6b suggests that

† In some references, a slightly different definition of W_r is used: k_r in eqn (8) is replaced by $\pi\bar{\kappa}$.[20]

‡ We do not consider the more complex shapes with several spherical invaginations.[11]

 This journal is © The Royal Society of Chemistry 2012

Published on 06 July 2012. Downloaded by Universitat Erlangen Nurnberg on 1/10/2020 8:46:35 AM.

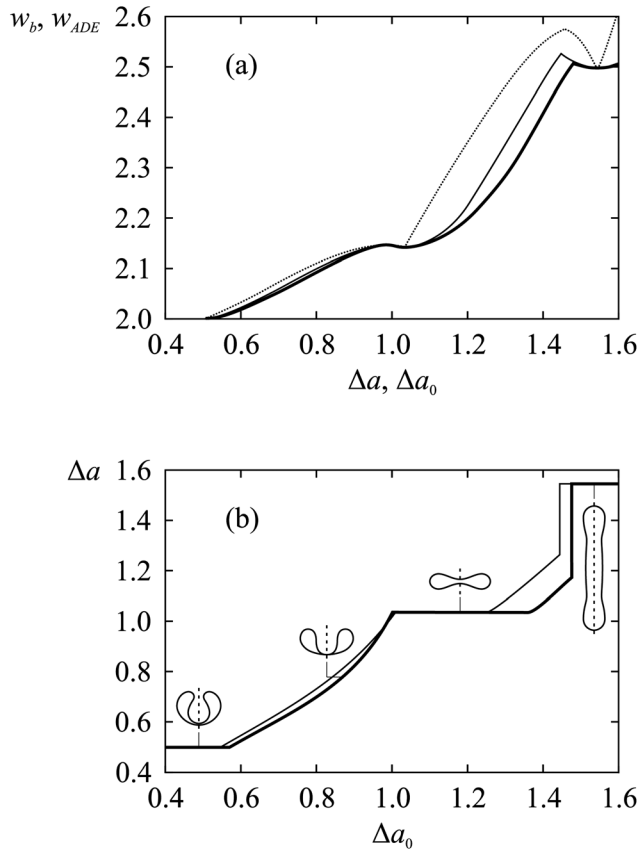

Fig. 6 Reduced ADE energy $w_{\mathrm{ADE}}(\Delta a_0)$ of the theoretical $v = 0.53$ vesicle *vs.* relaxed monolayer area difference Δa_0 for $q = 2$ and $q = 3$ [panel a: thick and thin lines, respectively; the reduced local bending energy $w_b(\Delta a)$ is plotted with the dashed line]. Panel b shows the dependence of Δa on Δa_0 for $q = 2$ (thick line) and $q = 3$ (thin line). Also shown are cross-sections of shapes with $\Delta a = 0.5$, 1.035, and 1.545 corresponding to the stomatocyte, the discocyte, and the cigar plateau and the $\Delta a = 0.80$ stomatocyte shape. Axes of symmetry are indicated by the dashed lines.

the role of the intermediate shapes depends on the ratio of the nonlocal and local bending constants, we may expect that this effect will be to some extent masked by the viscous damping mentioned above. This makes the duration of the discocyte phases reasonably well defined.

Let us begin with the $v = 0.51$ sequence. Guided by the results of ref. 9 we initially assumed that $\Delta a_0(t)$ is a linear function but we found that it cannot describe the data for any physically reasonable value of q because the duration of the cigar phase compared to the discocyte phase is too long. To explain the stagnant cigar phase, we must conclude that Δa_0 initially changes more slowly and that after some time it begins to decrease faster. Judging from experiments it is virtually impossible to exactly tell how this happens, but a quadratic functional form $\Delta a_0(t) = D_0 - D_1 t - D_2 t^2$ with a suitable choice of $D_i > 0$ works. In Fig. 7 we show a fit with $v_{\mathrm{ad}} = 0.53$, $q = 2$, $D_0 = 1.93$, $D_1 = 1 \times 10^{-4}\ \mathrm{s}^{-1}$, and $D_2 = 8 \times 10^{-5}\ \mathrm{s}^{-2}$. We stress that because of the cigar and the discocyte plateaux of $\Delta a(\Delta a_0)$, this particular dependence should be regarded solely as the simplest progressively steeper form of $\Delta a_0(t)$. Many other sets of D_i's and many other suitable concave decreasing functions of time would produce equally good agreement. With Fig. 7, we merely want to show that the experimental observations are consistent with the ADE theory.

Apart from showing that Δa_0 is not a linear function of time, the $v = 0.51$ transformation also imposes a rather strict upper bound on q. The sloping part of the step just before the discocyte plateau is only reproduced if q is smaller than about 2.5. For $q >$ 2.5, the sloping part would decay too slowly and there does not seem to exist a mechanism to compensate for this. On the other hand, a smaller value of $q < 2.5$ is reasonable, because the actual cigar–discocyte transition is smoothed and decelerated by viscous damping not included in the ADE theory. Thus our theoretical $\Delta a(t)$ curves should generally be more step-like than the experimental data. Our estimated upper bound of q is in very good agreement with tether-pulling experiments which suggest that $q \approx 2.4$ (ref. 26) and earlier studies of vesicle shape deformations where q was estimated to be 2.5 ± 1.[9]

As the elastic constants should be the same in all vesicles, we fit $v = 0.60$ and $v = 0.76$ sequences using the ADE theory with $q = 2$ (Fig. 7) so that the cigar–discocyte transition section of the theoretical $\Delta a(t)$ curves decays faster that the experimental curves, leaving some room for the viscous damping. The reduced volumes have been adjusted slightly to reproduce the cigar and the discocyte Δa plateaux. In these two vesicles $v_{\mathrm{ad}} = 0.61$ and $v_{\mathrm{ad}} = 0.77$, respectively, so that the correction needed $\Delta v = v_{\mathrm{ad}} - v = +0.01$ is positive as in the $v = 0.51$ vesicle where $\Delta v = +0.02$. This suggests that our image analysis protocol slightly underestimates the reduced volume of vesicles, which could be due to the shape fluctuations. Like in the $v = 0.51$ sequence, the $v = 0.61$ and the $v = 0.76$ sets of data cannot be described by a linear decrease of $\Delta a_0(t)$ but a quadratic form produces satisfactory fits.

The main conclusion of this analysis is that the step-like shape transformations are consistent with the ADE theory but that the time dependence of the preferred monolayer area difference is

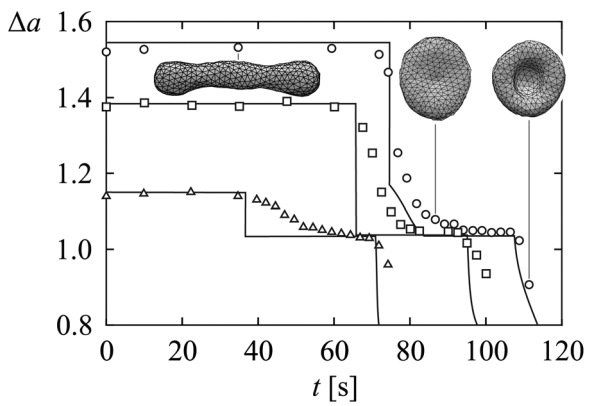

Fig. 7 Model of cigar–stomatocyte transition in vesicles of $v = 0.51$ (circles), $v = 0.60$ (squares), and $v = 0.76$ (triangles). Solid lines correspond to reduced monolayer area difference based on ADE theory with time-dependent Δa_0, and open symbols are the measured monolayer area difference Δa of the three shape sequences illustrated by three $v = 0.51$ shapes: A cigar, an asymmetric oblate shape, and a stomatocyte. The $v = 0.51$ sequence can only be described by ADE theory with $q \leq 2.5$; here we use $q = 2$ in all three fits. We assume that $\Delta a_0(t) = D_0 - D_1 t - D_2 t^2$. For $v = 0.51$, $v_{\mathrm{ad}} = 0.53$, $D_0 = 1.93$, $D_1 = 1 \times 10^{-4}\ \mathrm{s}^{-1}$, and $D_2 = 8 \times 10^{-5}\ \mathrm{s}^{-2}$; for $v = 0.60$, $v_{\mathrm{ad}} = 0.61$, $D_0 = 1.7$, $D_1 = 1.6 \times 10^{-4}\ \mathrm{s}^{-1}$, and $D_2 = 7.7 \times 10^{-4}\ \mathrm{s}^{-2}$; and for $v = 0.76$, $v_{\mathrm{ad}} = 0.77$, $D_0 = 1.1$, $D_1 = 9 \times 10^{-4}\ \mathrm{s}^{-1}$, and $D_2 = 9 \times 10^{-5}\ \mathrm{s}^{2}$.

Published on 06 July 2012. Downloaded by Universitat Erlangen Nurnberg on 1/10/2020 8:46:35 AM.

not linear. This is even more explicitly demonstrated by the bidirectional transformation shown in Fig. 8 where an asymmetric dumbbell vesicle of a reduced volume of $v = 0.58$ is transformed into a three-pearl necklace, a cigar, a racket, a discocyte, a stomatocyte, a discocyte, a triangular oblate shape, a three-arm starfish, and finally a four-pearl, three-arm budded shape. During this transformation where numerical image analysis was combined with estimated v and Δa of necklace and budded shapes (see Appendix A), Δa first briefly increases, then decreases, and finally it increases again to a value exceeding the initial monolayer area difference. This behavior can only be explained by a non-monotonic variation of Δa_0.

The bidirectional shape transformation offers ample insight into vesicle shape deformation. Firstly, we note that it is not reversible. The leg of the process leading from the necklace to the discocyte consists of racket shapes whereas the second leg where the discocyte is transformed into the three-arm budded shape involves triangular and starfish shapes. This is supported by the theoretically predicted discontinuity of the discocyte–cigar transition at reduced volumes below $v \approx 0.59$.[24] In this regime, the nonaxisymmetric shapes comprises the oblate/starfish and the prolate/racket branch, and each of these branches can be driven into the metastable regime. Since at $v \approx 0.58$ the transition between the two branches takes place at $\Delta a \approx 1.3$, the prolate/racket shapes that form the first part of the sequence are stable whereas the four-pearl, three-arm budded shapes seen in the final stage are metastable.

The reduced volume of the necklace and budded shapes computed by assuming that they consist of spherical buds (Appendix A) is systematically somewhat overestimated because the approximation used neglects the membrane area of the necks that connect the buds and the nonspherical shape of the buds itself. If this offset is taken into account, it is apparent that the reduced volume of the vesicle decreases slowly but steadily from $v \approx 0.58$ at $t = 0$ to $v \approx 0.55$ at $t = 350$ s. This rate of change seems too slow to drive any of the shape transformations observed.

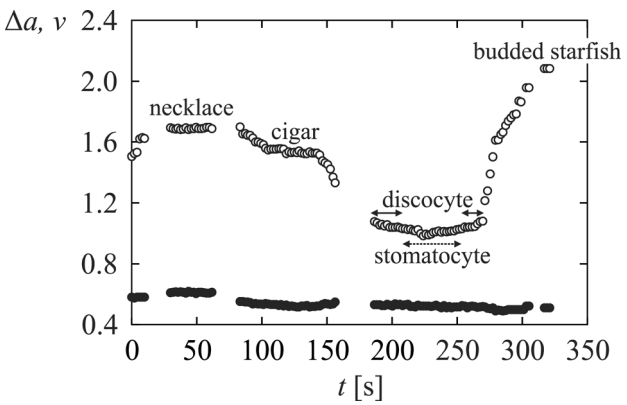

Fig. 8 Reduced monolayer area difference (open circles) and reduced volume (filled circles) of the bidirectional transformation of a $v = 0.58$ vesicle. The transformation includes a sequence of dumbbell, necklace, cigar, racket, discocyte, stomatocyte, discocyte, triangular oblate, three-arm starfish, and three-arm budded starfish shape; labeled are the plateaux representing the five persistent shapes. The reduced monolayer area difference varies in a non-monotonic step-like fashion, and the shapes observed are consistent with the discontinuous discocyte–cigar transition at small enough reduced volumes. The reduced volume slowly decreases with time. The gaps between the datapoints are of a technical nature. The recorded movies need to be saved from time to time, and further recording is not possible during saving.

4.2. Origin of shape transformations

Some shape deformations reported here have been observed in the past. By changing the temperature of the solution of lecithin vesicles,[19] discocytes were transformed into stomatocytes and budding was induced in elliptocytes. The underlying variation of Δa_0 was attributed to the differential temperature expansivity of the inner and the outer monolayer, which was assumed to vary from vesicle to vesicle.[19] The observed trajectories in the (v, Δa)-plane generally did not take place at fixed reduced volume.[4,19] Certain time dependences of Δa_0 can be associated with flip-flops of lipids from one monolayer to the other. This relaxation process may be effective in shape transformations where the vesicle energy is decreased, say in the discocyte–stomatocyte transition at $v < 0.6$. In shape deformations of vesicles transferred to pure water, the decrease of Δa_0 with time was interpreted in terms of dissolution of lipids from the outer monolayer which is supposedly driven by the low concentration of lipids in the surrounding water.[9]

In our experiments, we did not vary the temperature nor did we put the vesicles in an environment where the concentration of lipids would be low. Yet shape deformations did take place, and their sense could not be associated with an easily identifiable external stimulus. We are led to conjecture that Δa_0 is controlled by a microscopic mechanism beyond the resolution of optical microscope. One possibility is that either the inner or the outer monolayers have one or more small reservoirs of lipids in the form of folds formed during the rehydration of dried lipid film.[27] Should these reservoirs unfold, the area of the corresponding monolayer would increase, thereby changing the relaxed monolayer area difference. Releasing lipids from folds on the inner and outer monolayer would make the monolayer area difference decrease and increase, respectively.

Of course, an increase of the area of either monolayer would also lead to a decrease of the reduced volume but as shown in Appendix B this effect is rather small compared to the variation of Δa_0 so that in the zero-order approximation v can be assumed constant. Still in the long-lasting shape transformations involving considerable changes of Δa_0, a certain variation of v may be seen. For example, during the bidirectional shape transformation shown in Fig. 8 the reduced volume decreased from ≈ 0.58 to ≈ 0.55. In this transformation, the total change of Δa_0 is of the order of 1 and according to arguments presented in Appendix B, a part of the decrease of v can indeed be associated with an increased monolayer area due to the release of lipids from the folds.

The fold hypothesis is consistent with several observations of ours. Firstly, a given vesicle could be formed with folds on both monolayers, which would make it capable of performing shape deformations in either direction. Secondly, folds are internal structures unrelated to ambient conditions and thus they can account for the diverging shape transformations of very similar vesicles located in the same environment such as the two cigars shown in Fig. 2. Thirdly, the shape transformations are sporadic

 This journal is © The Royal Society of Chemistry 2012

Published on 06 July 2012. Downloaded by Universitat Erlangen Nurnberg on 1/10/2020 8:46:35 AM.

and seemingly unprovoked by an external stimulus as if the fold remained in a dormant state until a random perturbation triggered the unfolding. Indeed, some vesicles underwent shape transformations after long waiting periods of up to 160 s. Lastly, the most plausible dynamics of monolayer area increase due to release of lipids from folds seems to be burst-like rather than continuous, which would lead to a staggered temporal variation of Δa_0. These dynamics would further contribute to the step-like evolution of vesicle shape described by $\Delta a(t)$, which would thus be caused both by the ADE elasticity and the unsteady increase of areas of the inner and the outer monolayers. All of the above facts indirectly support the existence of folds.

5. Conclusions

In this study, we used a confocal microscope to study the shape of giant unilamellar lipid vesicles. We developed custom image-processing software and used it in conjunction with Surface Evolver to analyze the vesicle shapes in detail. With our methodology, we were able to extract the full 3D shape of axisymmetric and nonaxisymmetric vesicles of arbitrary orientation, thereby considerably surpassing the scope of the more common phase-contrast microscopy.

3D imaging is instrumental in the analysis of nonaxisymmetric shapes and we used it to systematically explore the phase diagram. Our vesicles underwent spontaneous shape transformations and by monitoring them we recorded the various types of simple axisymmetric shapes (stomatocytes, discocytes, cigars, pearl necklaces) as well as many nonaxisymmetric shapes including elliptocytes, rackets, triangular oblate shapes, starfish, and budded shapes; also observed was a range of more complex morphologies (Fig. 9).[28] Almost all genus-0 vesicles studied agree with the bilayer-couple theory, fitting nicely into the theoretical phase diagram.

On the other hand, the shape transformations were staggered rather than gradual, which can be interpreted in terms of the area-difference-elasticity theory.[9] Our study shows that the discontinuous transitions predicted by the area-difference-elasticity theory are materialized by a sequence of bilayer-couple shapes connecting the two stable states. More importantly, the direction of the shape transformations seemed to be arbitrary so that in some cases invaginated shapes evolved into convex shapes and in others they evolved in the opposite direction. Some vesicles even exhibited bidirectional shape transformations. These experimental observations point to the possibility that the transformations were caused by the release of lipids from folds formed during rehydration of the dried lipid film, suggesting that they need not be driven by an external stimulus such as changing temperature.

The level of detail of the reported results, especially the full 3D description of the nonaxisymmetric shapes, relies on the experimental methodology developed in this study. Here we tested it on simple vesicles but in the future we will use it for investigations of transformations in complex vesicular systems such as budding in ternary vesicles,[29,30] pore opening,[31,32] and vesicle self-reproduction.[33] In these processes, a quantitative insight into the evolving shapes of vesicles is crucial for the identification of the driving forces and the mechanisms at work.

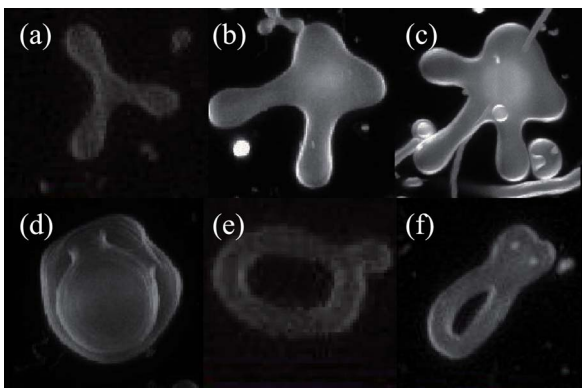

Fig. 9 Complex shapes observed: Apart from the three-armed starfishes (a), also seen were related shapes with two (b) or three arms (c) and a prolate body. The bottom row shows shapes of non-zero genus: A two-neck stomatocytes of doughnut topology (d), a degenerate two-hole figure-of-eight shape with one large and one large ring (e) and a related three-hole shape (f).

Appendix A: Morphometric parameters of budded shapes

In the case of pearl necklace vesicles and other shapes composed of buds, the reduced volume and the reduced monolayer area difference can be estimated easily.[11] We assume that the buds are spherical and neglect the necks that connect them. The total area of N buds of radii $R_1, R_2, \ldots R_N$ is

$$A = 4\pi \sum_{i=1}^{N} R_i^2 \tag{11}$$

and their total volume reads

$$V = \frac{4\pi}{3} \sum_{i=1}^{N} R_i^3. \tag{12}$$

The monolayer area difference of a single bud of radius R_i is $\Delta A_i = h\oint(C_1 + C_2)\mathrm{d}A = 8\pi h R_i$ [eqn (4)] so that for a shape consisting of N buds

$$\Delta A = 8\pi h \sum_{i=1}^{N} R_i. \tag{13}$$

From the total area, we first compute R_s needed to normalize ΔA and V [eqn (5) and (6)]:

$$R_s = \sqrt{\frac{A}{4\pi}} = \sqrt{\sum_{i=1}^{N} R_i^2}. \tag{14}$$

Thus the reduced volume of the budded shape is

$$v = \frac{V}{4\pi R_s^3/3} = \frac{\sum_{i=1}^{N} R_i^3}{\sqrt{\sum_{i=1}^{N} R_i^2}^3}, \tag{15}$$

whereas its reduced monolayer area difference reads

$$\Delta a = \frac{\Delta A}{8\pi h R_s} = \frac{\sum_{i=1}^{N} R_i}{\sqrt{\sum_{i=1}^{N} R_i^2}}. \tag{16}$$

Published on 06 July 2012. Downloaded by Universitat Erlangen Nurnberg on 1/10/2020 8:46:35 AM.

Using eqn (15) and (16), v and Δa of a budded shape can be readily computed from the radii of the buds. Given that the actual shape of the buds is prolate rather perfectly spherical, eqn (15) somewhat overestimates the reduced volume whereas the reduced monolayer area difference is underestimated by eqn (16).

Appendix B: Variation of v and Δa upon release of lipids from folds

Let us estimate the relative variation of reduced volume and reduced monolayer area difference after the inner or the outer monolayer area has been increased due to the postulated unfolding of the folds. In terms of the areas of the outer and the inner monolayers (A_o and A_i, respectively) the reference area of the membrane before the release is given by

$$A' = \frac{A_o + A_i}{2}. \tag{17}$$

Now assume that the areas of the outer and the inner monolayers change by δA_o and δA_i, respectively. The corresponding change of membrane area is $\delta A = (\delta A_o + \delta A_i)/2$ so that the reduced volume defined by eqn (5) where $R_s = \sqrt{A/4\pi}$ and $A = A' + \delta A$ is

$$\begin{aligned} v &= \frac{3V}{4\pi\sqrt{(A'+\delta A)/4\pi}^3} = \frac{3V}{4\pi\sqrt{A'/4\pi}^3\sqrt{1+\delta A/A'}^3} \\ &\approx \frac{3V}{4\pi\sqrt{A'/4\pi}^3}\left(1 - \frac{3}{4}\frac{\delta A_o + \delta A_i}{A'}\right) \\ &\approx v'\left(1 - \frac{3}{4}\frac{\delta A_o + \delta A_i}{A'}\right). \end{aligned} \tag{18}$$

Here the reduced volume was expanded in terms of relative monolayer area changes $\delta A_o/A'$ and $\delta A_i/A'$.

Next we compute the variation of the reduced monolayer area difference. The reference area difference $\Delta A' = A_o - A_i$ corresponds to

$$\Delta a_0' = \frac{A_o - A_i}{8\pi h\sqrt{A'/4\pi}} = \frac{\Delta A_0'}{8\pi h\sqrt{A'/4\pi}}. \tag{19}$$

After release the reduced monolayer area difference reads

$$\begin{aligned} \Delta a_0 &= \frac{A_o + \delta A_o - A_i - \delta A_i}{8\pi h\sqrt{(A'+\delta A)/4\pi}} = \frac{\Delta A_0'\left[1 + (\delta A_o - \delta A_i)/\Delta A'\right]}{8\pi h\sqrt{A'/4\pi}\sqrt{1+\delta A/A'}} \\ &\approx \Delta a_0'\left(1 + \frac{\delta A_o - \delta A_i}{\Delta A_0'}\right)\left(1 - \frac{1}{4}\frac{\delta A_o + \delta A_i}{A'}\right). \end{aligned} \tag{20}$$

(In the last step, we expanded the denominator to the lowest order in $\delta A/A'$.)

These results can be used to evaluate the effect of the release of lipids from a fold on the outer monolayer. In this case $\delta A_o > 0$ and $\delta A_i = 0$. We compare the corresponding relative variation of reduced volume and reduced monolayer area difference at a given relative monolayer area increase $\delta A_o/A'$. From eqn (18) we find that

$$\frac{\delta v}{v'} = \frac{v - v'}{v'} = -\frac{3}{4}\frac{\delta A_o}{A'} \tag{21}$$

and eqn (20) gives

$$\frac{\delta(\Delta a_0)}{\Delta a_0'} = \frac{\Delta a_0 - \Delta a_0'}{\Delta a_0'} \approx \left(\frac{A'}{\Delta A_0'} - \frac{1}{4}\right)\frac{\delta A_o}{A'}. \tag{22}$$

We see that $\delta v/v'$ is of the same order as $\delta A_o/A'$ whereas $\delta(\Delta a_0)/\Delta a_0$ is much bigger because $A'/\Delta A_0'$ is typically $\sim$1000. This can be verified easily: $A'/\Delta A_0' \sim 4\pi R_s^2/8\pi h R_s \sim R_s/2h$ and since membrane thickness h is a few nm and vesicle size is a few μm, $A'/\Delta A_0' \sim 1000$.

The above argument shows that the relative change of the area of the outer monolayer $\delta A_o/A'$ affects the reduced monolayer area difference rather dramatically but the corresponding reduced volume change is much smaller. This is the reason why the shape transformations take place at an almost constant reduced volume. Analogous reasoning applies to the inner monolayer.

The proposed release of lipids from folds is very similar to the theory based on differential thermal expansivity of the monolayers[4] in that they both give rise to shape transformation trajectories that take place at a virtually constant reduced volume [see, *e.g.*, curves (1) and (2) in Fig. 12 in ref. 4].

Acknowledgements

It is our pleasure to acknowledge numerous discussions with S. Svetina, and we thank J. Majhenc and A. Lošdorfer Božič for helpful suggestions. This work was supported by KAKENHI (Grant-in-Aid for Scientific Research) on the Priority Area "Soft Matter Physics" from the MECSST, by Grant-in-Aid for Scientific Research (A) no. 22244053 from the Japan Society for the Promotion of Science, by the JSPS International Training Program (ITP), by Slovenian Research Agency through Grant no. P1-0055 and by the Marie-Curie Initial Training Network COMPLOIDS under FP7-PEOPLE-ITN-2008 Grant no. 234810.

References

1 S. Mogelsvang, B. J. Marsh, M. S. Ladinsky and K. E. Howell, *Traffic*, 2004, **5**, 338–345.
2 D. M. Shotton, *J. Cell Sci.*, 1989, **94**, 175–206.
3 H. Hotani, *J. Mol. Biol.*, 1984, **178**, 113–120.
4 J. Käs and E. Sackmann, *Biophys. J.*, 1991, **60**, 825–844.
5 J. Käs, E. Sackmann, R. Podgornik, S. Svetina and B. Žekš, *J. Phys. II*, 1993, **3**, 631–645.
6 W. Wintz, H.-G. Döbereiner and U. Seifert, *Europhys. Lett.*, 1996, **33**, 403–408.
7 H.-G. Döbereiner, E. Evans, M. Kraus, U. Seifert and M. Wortis, *Phys. Rev. E: Stat. Phys., Plasmas, Fluids, Relat. Interdiscip. Top.*, 1997, **55**, 4458–4474.
8 H. Hotani, F. Nomura and Y. Suzuki, *Curr. Opin. Colloid Interface Sci.*, 1999, **4**, 358–368.
9 J. Majhenc, B. Božič, S. Svetina and B. Žekš, *Biochim. Biophys. Acta, Gen. Subj.*, 2004, **1664**, 257–266.
10 W. Helfrich, *Z. Naturforsch., A: Phys., Phys. Chem., Kosmophys.*, 1973, **28c**, 693–703.
11 S. Svetina and B. Žekš, *Eur. Biophys. J.*, 1989, **17**, 101–111.
12 U. Seifert, K. Berndl and R. Lipowsky, *Phys. Rev. A: At., Mol., Opt. Phys.*, 1991, **44**, 1182–1202.
13 U. Seifert, *Adv. Phys.*, 1997, **46**, 13–137.
14 V. Heinrich, S. Svetina and B. Žekš, *Phys. Rev. E: Stat. Phys., Plasmas, Fluids, Relat. Interdiscip. Top.*, 1993, **48**, 3112–3123.
15 X. Michalet, *Phys. Rev. E: Stat., Nonlinear, Soft Matter Phys.*, 2007, **76**, 021914.

 This journal is © The Royal Society of Chemistry 2012

Published on 06 July 2012. Downloaded by Universitat Erlangen Nurnberg on 1/10/2020 8:46:35 AM.

16 P. M. Vlahovska, R. S. Gracià, S. Aranda-Espinoza and R. Dimova, *Biophys. J.*, 2009, **96**, 4789–4803.
17 V. Heinrich, F. Sevšek, S. Svetina and B. Žekš, *Phys. Rev. E: Stat. Phys., Plasmas, Fluids, Relat. Interdiscip. Top.*, 1997, **55**, 1809–1818.
18 M. Wortis, M. Jarić and U. Seifert, *J. Mol. Liq.*, 1997, **71**, 195–207.
19 K. Berndl, J. Käs, R. Lipowsky, E. Sackmann and U. Seifert, *Europhys. Lett.*, 1990, **13**, 659–664.
20 L. Miao, U. Seifert, M. Wortis and H.-G. Döbereiner, *Phys. Rev. E: Stat. Phys., Plasmas, Fluids, Relat. Interdiscip. Top.*, 1994, **49**, 5389–5407.
21 J. P. Reeves and R. M. Dowben, *J. Cell. Physiol.*, 1969, **73**, 49–60.
22 D. Needham and E. Evans, *Biochemistry*, 1988, **27**, 8261–8269.
23 K. Brakke, *Exp. Math.*, 1992, **1**, 141–165; the software package is available free of charge at http://www.susqu.edu/brakke/evolver/evolver.html.
24 P. Ziherl and S. Svetina, *Europhys. Lett.*, 2005, **70**, 690–696.
25 S. Svetina and B. Žekš, *Anat. Rec.*, 2002, **268**, 215–225.
26 S. Svetina, B. Žekš, R. E. Waugh and R. M. Raphael, *Eur. Biophys. J.*, 1998, **27**, 197209.
27 R. Bar-Ziv, E. Moses and P. Nelson, *Biophys. J.*, 1998, **75**, 294–320.
28 X. Michalet and D. Bensimon, *Science*, 1995, **269**, 666–668.
29 T. Baumgart, S. T. Hess and W. W. Webb, *Science*, 2003, **425**, 821–824.
30 M. Yanagisawa, M. Imai and T. Taniguchi, *Phys. Rev. Lett.*, 2008, **100**, 148102.
31 M. Ohno, T. Hamada, K. Takaguchi and M. Homma, *Langmuir*, 2009, **25**, 11680–11685.
32 Y. Sakuma, T. Taniguchi and M. Imai, *Biophys. J.*, 2010, **99**, 472–479.
33 Y. Sakuma and M. Imai, *Phys. Rev. Lett.*, 2011, **107**, 198101.